Matter

CellPress
OPEN ACCESS

Article

Liquid-like Interfaces Mediate Structural Phase Transitions in Lead Halide Perovskites

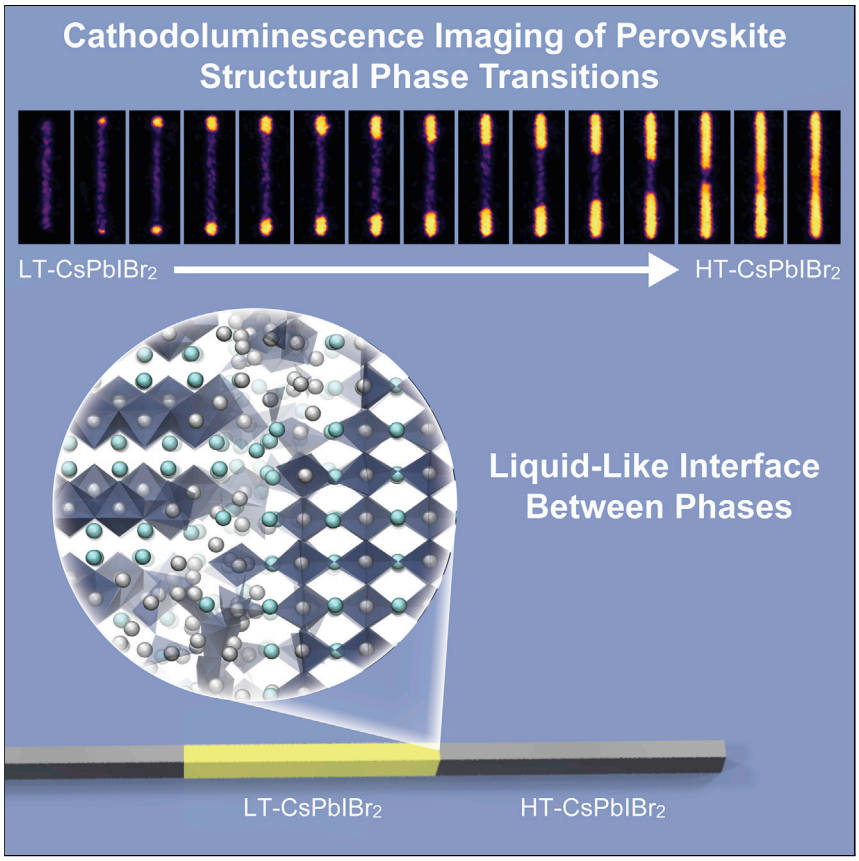

Understanding and controlling structural phase transitions in metal halide perovskites is important for designing stable and efficient optoelectronic devices. Using *in situ* nanoscale cathodoluminescence microscopy, we visualize the thermally driven transition to the perovskite phase in $CsPbIBr_2$ nanowires. Combined with molecular simulation, we reveal that the transformation proceeds despite a substantial energy barrier via ion diffusion through a liquid-like interface between the two structures. While cations disorder in this liquid-like region, the halide ions retain substantial spatial correlations to template the perovskite phase.

Connor G. Bischak, Minliang Lai, Zhaochuan Fan, ..., David T. Limmer, Peidong Yang, Naomi S. Ginsberg

dlimmer@berkeley.edu (D.T.L.)
p_yang@berkeley.edu (P.Y.)
nsginsberg@berkeley.edu (N.S.G.)

HIGHLIGHTS

Halide ion diffusion mediates $CsPbIBr_2$ double-chain to perovskite phase transition

EM and *in situ* CL microscopy of $CsPbIBr_2$ nanowires characterize structural transition

MD simulation shows disorder yet correlations at interface boundary between phases

Disorder and diffusion aid to overcome the sizable energy barrier for the transition

3 **Understanding**
Dependency and conditional studies on material behavior

Bischak et al., Matter *3*, 534–545
August 5, 2020
https://doi.org/10.1016/j.matt.2020.07.015

CellPress
OPEN ACCESS

Matter

Article

Liquid-like Interfaces Mediate Structural Phase Transitions in Lead Halide Perovskites

Connor G. Bischak,[1,14] Minliang Lai,[1,14] Zhaochuan Fan,[2,14] Dylan Lu,[1] Philippe David,[2] Dengpan Dong,[8] Hong Chen,[1,9] Ahmed S. Etman,[10,11] Teng Lei,[1] Junliang Sun,[12] Michael Grünwald,[2] David T. Limmer,[1,3,5,*] Peidong Yang,[1,3,5,7,*] and Naomi S. Ginsberg[1,3,4,5,6,13,15,*]

SUMMARY

Microscopic pathways of structural phase transitions in metal halide perovskites are difficult to probe because they occur over disparate time and length scales and because electron-based microscopies typically used to directly probe nanoscale dynamics of phase transitions often damage metal halide perovskite materials. Using *in situ* nanoscale cathodoluminescence microscopy with low electron beam exposure, we visualize nucleation and growth in the thermally driven transition to the perovskite phase in hundreds of non-perovskite phase nanowires. In combination with molecular dynamics simulations, we reveal that the transformation does not follow a simple martensitic mechanism, but proceeds despite a substantial energy barrier via ion diffusion through a liquid-like interface between the two structures. While cations are disordered in this liquid-like region, the halide ions retain substantial spatial correlations. This detailed picture not only reveals how phase transitions between disparate structures can proceed, but also opens the possibility to control such processes.

INTRODUCTION

Metal halide perovskites are promising semiconductor materials for optoelectronics,[1–5] and are an ideal platform for investigating solid-solid phase transitions.[6–9] Metal halide perovskites undergo numerous structural phase transitions that affect their optoelectronic properties.[7,8,10] One significant structural phase transition is between the perovskite phase and so-called "yellow" non-perovskite phase of $CsPbI_3$.[6,11] Numerous efforts have aimed to stabilize the perovskite phase of $CsPbI_3$,[12–15] which is thermodynamically unstable at room temperature and ambient pressure.[16] Much like $CsPbI_3$, the metal halide perovskite material, $CsPbIBr_2$, undergoes a thermally driven phase transition from a low-temperature non-perovskite phase (LT-$CsPbIBr_2$) to a high-temperature perovskite phase (HT-$CsPbIBr_2$) upon heating (Figure 1A). $CsPbIBr_2$ is kinetically trapped in the HT-$CsPbIBr_2$ phase upon cooling, and the phase transition is therefore typically not reversible, although its transition back to the LT-$CsPbIBr_2$ phase can be catalyzed by humidity.[9] This phase transition contributes to the instability of perovskite photovoltaics[6,17] and has been utilized for generating nanoscale p-n heterojunctions[18] and thermochromic smart window technologies.[9] Despite much interest, the mechanism of this phase transition has not been explained. In contrast to structurally similar perovskite phases known to interconvert,[7,19] LT-$CsPbIBr_2$ and HT-$CsPbIBr_2$ are not related by simple elastic deformations. Transitions between these dissimilar lattices thus require a more complex rearrangement of atoms, suggesting the possibility to observe a diffusive transformation and to evaluate how the anharmonic, soft, and ionic nature

Progress and Potential

Controlling structural phase transitions in solid-state devices is vital to ensure stable and efficient devices. Metal halide perovskites are semiconductors of high interest for photovoltaic and light-emitting applications, yet unintended conversion from the so-called "black" perovskite phase to a "yellow" non-perovskite phase leads to poor device efficiency and stability. This work visualizes the kinetics of the structural phase transition between the two phases in $CsPbIBr_2$ nanowires via *in situ* nanoscale cathodoluminescence imaging. Together with molecular dynamics simulations, we provide a comprehensive picture of how the structural transition progresses, revealing a liquid-like interface between the perovskite and non-perovskite phases whose disorder aids to overcome the sizable activation barrier that we measure. This new understanding should guide the design of more stable and efficient halide perovskite materials, which already show high promise for next-generation electronics.

of the material affects its dynamics.[20] Additionally, the volume of the material increases by approximately 7% during the transition from LT-$CsPbI_3$ to HT-$CsPbI_3$,[21] suggesting that disparate interfacial energies and lattice strain could play an important role in nucleation and growth.

Direct, non-invasive imaging of structural changes is challenging in relatively delicate materials such as metal halide perovskites. For instance, structural phase transitions are often probed using bulk characterization techniques, such as *in situ* X-ray diffraction (XRD),[22–24] yet these techniques average over microscopic dynamics. On the other hand, transmission electron microscopy (TEM) has been used to directly image structural phase transitions with atomic resolution,[25,26] yet the high electron beam dose is only compatible with select hard materials and beam-induced damage precludes prolonged imaging of metal halide perovskites. Cathodoluminescence (CL) microscopy uses a focused, scanning electron beam to excite the sample of interest, and the emitted light is collected by a parabolic mirror and directed to a detector to form an image (Figure 1B). Previously, CL microscopy has been used to image steady-state properties[18,27–31] and dynamic processes[32,33] of metal halide perovskites. Because of the low current and accelerating voltage of the electron beam, sample damage is limited even at relatively high temperatures in comparison with typical TEM studies.[34] Compared with optical microscopies, such as photoluminescence (PL) microscopy, the key benefits of CL imaging are its higher spatial resolution, multiscale nature (tens-of-nanometers resolution to hundreds-of-micrometers field of view), and, most importantly, its ability to easily spatially correlate the high-resolution structural information, found in the secondary electron images obtained in tandem, to the optical CL emission maps.

Here we reveal the mechanism of an important yet heretofore elusive non-martensitic, diffusive structural transformation in an ionic alkali metal halide semiconductor on the nanoscale by exploiting differences in CL emission of different crystal structures and combining those observations with molecular dynamics (MD) simulations and coarse-grained models. With low-dose *in situ* scanning electron CL imaging, we follow the structural transformation in $CsPbIBr_2$ nanowires with high temporal and spatial resolution over a large field of view, allowing the simultaneous characterization of the nucleation and growth kinetics in a statistically significant number of single particles. The multiple scales covered by our experimental observations and modeling enable us to determine the microscopic mechanisms of the structural transformation. We find that both nucleation and growth are characterized by strongly anisotropic kinetics and that the boundary between crystal structures is propagated by activated ion diffusion through a thin, yet finite, liquid-like interface. Despite the overall disorder of the interface, long-range anionic charge density correlations are observed, suggesting that they promote the crystallographic registration of the two crystal phases. Our observations provide a detailed view of the complex dynamic pathways by which two distinct crystal structures interconvert.

RESULTS AND DISCUSSION

We use CL imaging with *in situ* heating to monitor the phase-transition kinetics of $CsPbIBr_2$. Similarly to $CsPbI_3$ nanowires, single-crystal LT-$CsPbIBr_2$ nanowires were synthesized with the edge-sharing octrahedral chains oriented along the long axis of the nanowires, as confirmed by continuous rotation electron diffraction (cRED) (Figure S1). Helpful to this study, the LT-$CsPbIBr_2$ phase has an indirect band gap, resulting in low PL emission, whereas the direct bandgap HT-$CsPbIBr_2$ phase exhibits bright PL emission (Figure 1C). This large difference in emission intensity produces strong contrast

[1]Department of Chemistry, University of California, Berkeley, CA 94720, USA

[2]Department of Chemistry, University of Utah, Salt Lake City, UT 84112, USA

[3]Materials Sciences Division, Lawrence Berkeley National Laboratory, Berkeley, CA 94720, USA

[4]Department of Physics, University of California, Berkeley, CA 94720, USA

[5]Kavli Energy NanoScience Institute, Berkeley, CA 94720, USA

[6]Molecular Biophysics and Integrated Bioimaging Division, Lawrence Berkeley National Laboratory, Berkeley, CA 94720, USA

[7]Department of Materials Science and Engineering, University of California, Berkeley, CA 94720, USA

[8]Department of Materials Science and Engineering, University of Utah, Salt Lake City, UT 84112, USA

[9]School of Environmental Science and Engineering, Southern University of Science and Technology, Shenzhen, Guangdong, China

[10]Department of Materials and Environmental Chemistry (MMK), Stockholm University, Stockholm 106 91, Sweden

[11]Department of Chemistry, Faculty of Science, Alexandria University, Ibrahimia, Alexandria 21321, Egypt

[12]College of Chemistry and Molecular Engineering, Peking University, Beijing 100871, China

[13]STROBE NSF Science & Technology Center, Berkeley, CA 94720, USA

[14]These authors contributed equally

[15]Lead Contact

*Correspondence:
dlimmer@berkeley.edu (D.T.L.),
p_yang@berkeley.edu (P.Y.),
nsginsberg@berkeley.edu (N.S.G.)

https://doi.org/10.1016/j.matt.2020.07.015

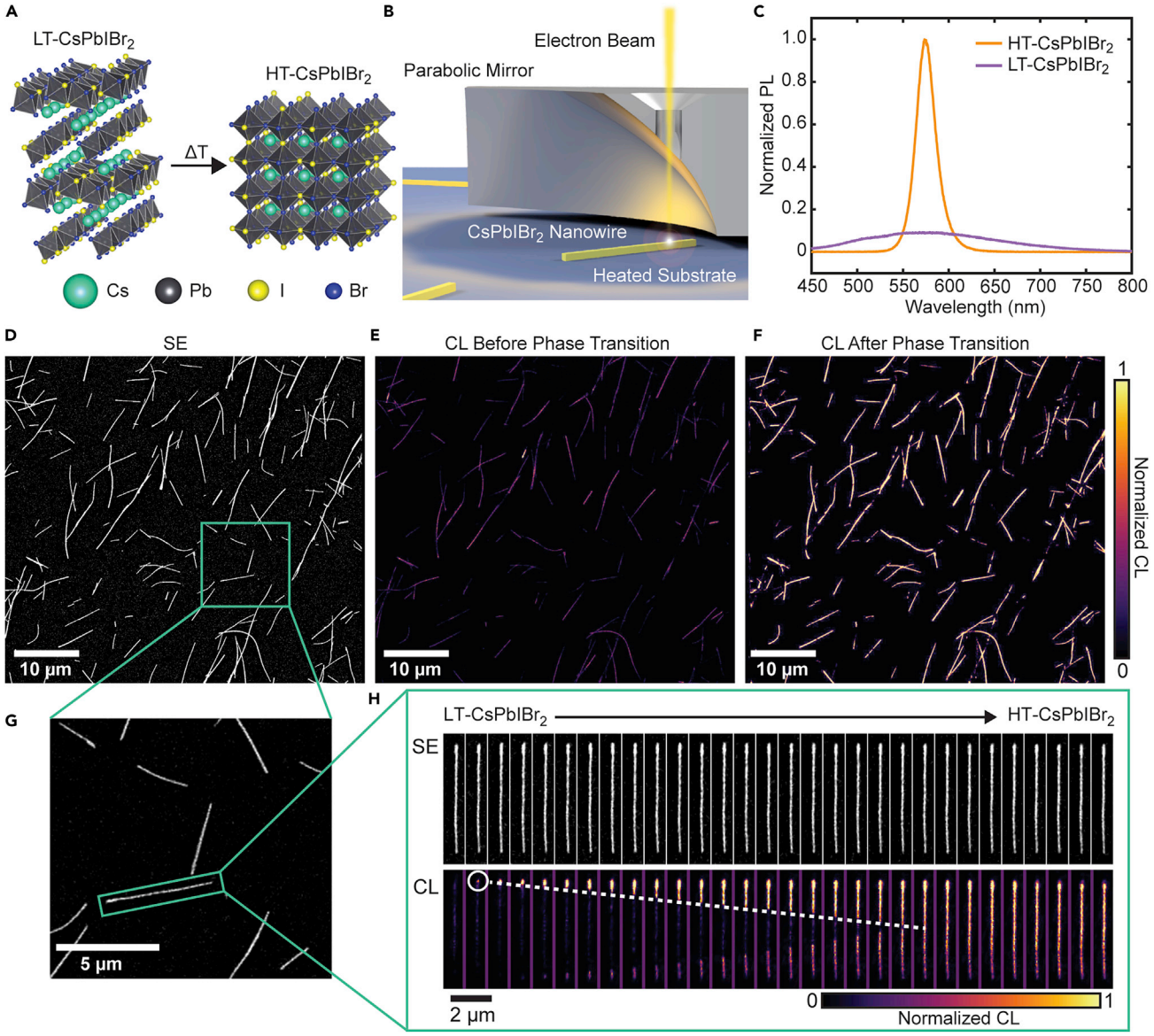

Figure 1. Cathodoluminescence Imaging of the LT-$CsPbIBr_2$ to HT-$CsPbIBr_2$ Phase Transition in Nanowires

(A) Schematic of the LT-$CsPbIBr_2$ and HT-$CsPbIBr_2$ phases.

(B) Schematic of the CL imaging apparatus.

(C) Photoluminescence spectra of LT-$CsPbIBr_2$ and HT-$CsPbIBr_2$ nanowires.

(D–F) (D) SE image of the full field of view of the measurement containing ~150 individual nanowires. Scale bar, 10 μm. CL images (E) before and (F) after the phase transition. Scale bars, 10 μm.

(G) Magnified view showing individual nanowires. Scale bar, 5 μm.

(H) An example time series of SE and CL images of the single nanowire in (G) during the phase transition using a 163°C setpoint. The white circle indicates one of two nucleation events in the nanowire, and the dotted white line marks the corresponding phase boundary as it migrates along the length of the nanowire. Adjacent snapshots are separated in time by 6 s. Scale bar, 2 μm.

See also Figure S5.

differences between the two structures during CL imaging and allows us to accurately track the progress of the phase transition at high resolution.

The combination of the nanowire geometry and the high spatial resolution of CL imaging allows for a quantitative analysis of the phase-propagation rates along the

length of the nanowire. The quasi-one-dimensional sample geometry of the nanowires enables straightforward tracking of a single interphase boundary along a single axis, uncomplicated by grain boundaries or variations in defect concentration found in polycrystalline lead halide perovskite thin films. The transverse wire dimensions are also large enough to study intrinsic properties without introducing quantum confinement effects, and we do not expect the thermodynamics of the phase transition to differ from those of a bulk sample.

Using CL microscopy, we measure a large field of view containing tens to hundreds of these $CsPbIBr_2$ nanowires to build up statistics on nucleation and growth kinetics. A secondary electron (SE) image of a typical field of view is shown in Figure 1D, containing ~150 nanowires that are monitored simultaneously; CL images showing the nanowires before and after the phase transition are shown in Figures 1E and 1F, respectively. The evolution of the nanowires from the LT-$CsPbIBr_2$ to the HT-$CsPbIBr_2$ phase from this larger field of view is depicted in Figure S2A and Video S1. Without heating, we do not observe the phase transition upon repeated CL imaging (Figure S2B). We select individual nanowires from this larger field of view (Figure 1G) and measure phase-propagation rates. Figure 1H shows a time series of simultaneously acquired SE and CL images that illustrate the evolution from LT-$CsPbIBr_2$ to HT-$CsPbIBr_2$ in a single nanowire upon heating. Although no changes are obvious in the SE images, the CL images initially show a nanowire entirely composed of LT-$CsPbIBr_2$ followed by nucleation of the bright HT-$CsPbIBr_2$ phase at the nanowire ends and phase propagation along the length of the wire until the wire is completely converted to HT-$CsPbIBr_2$. The CL intensity as a function of time and distance along the wire axis is shown for this process in Figure S2C. Temperature-dependent *in situ* XRD before and after the phase transition confirms the presence of the two phases (Figure S3).

Taking advantage of the ability to probe the phase-transition dynamics in many $CsPbIBr_2$ nanowires simultaneously, we provide a statistical analysis of the HT-$CsPbIBr_2$ phase growth rate as a function of temperature. We record the phase-propagation dynamics of a population of nanowires at temperatures ranging from 163°C to 182°C. To do so, we first rapidly increase the stage temperature to a given set point. Stage temperature equilibration occurs fast enough (a few tens of seconds, Figure S4) that we are able to subsequently capture the initial stages of the phase transition. By following the phase boundary propagation over a few minutes, we determine the ~constant phase-propagation rate in each nanowire, considering frames only once the stage is maintaining a constant temperature (see Supplemental Information and Figure S5 for more details). Figure 2A shows the distribution of phase-propagation rates at three different temperatures with typical time series of individual nanowires shown in the inset. At 163°C, 177°C, and 182°C, we observe average propagation rates of 3.1 ± 0.2 nm/s, 11 ± 1 nm/s, and 33 ± 3 nm/s, respectively. We do not observe any dependence of the propagation rate on either nanowire length or diameter. The strong temperature dependence of the propagation rate, combined with the increase of the rate distribution widths with temperature, suggests that phase propagation is controlled by thermally activated microscopic processes. Indeed, we find that the propagation rate as a function of temperature exhibits Arrhenius-like behavior with an activation energy of 210 ± 60 kJ/mol (Figure 2B), about 50-times the scale of a typical thermal fluctuation (k_BT). (Uncertainty provided represents 95% confidence interval.) Given this substantial energetic barrier, there must be a significant compensating increase in entropy for interphase boundary propagation to proceed at the observed rates.

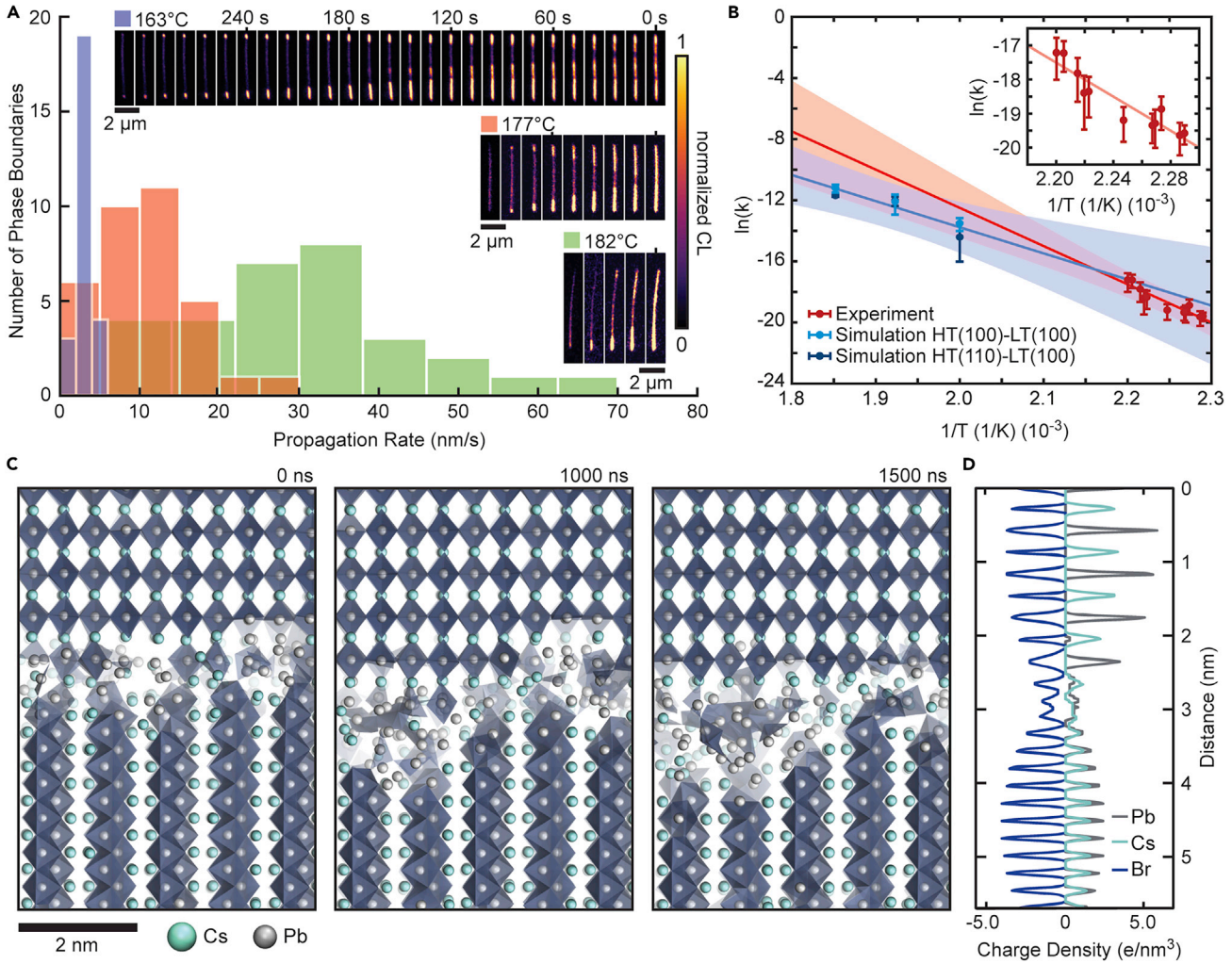

Figure 2. Energetics of Perovskite Phase Propagation

(A) Histograms of the propagation rate of three different populations of nanowires heated at three different constant temperatures, 163°C (purple), 177°C (orange), and 182°C (green). The insets show a characteristic nanowire at each temperature with a countdown time axis for full conversion to the perovskite phase shown at the top. Scale bars, 2 μm.

(B) Arrhenius plot of experimental and MD simulation data. Red points correspond to the experimental propagation rate of different nanowire populations measured at different temperatures, where the units of k are m/s, also shown in the inset; from the simulation data, light-blue points indicate growth rates of <100> HT-$CsPbBr_3$ along the wire axis, as observed in cRED and SAED (Figure S1), and dark blue points indicate growth rates of <110> HT-$CsPbBr_3$ along the wire axis. Data are presented as mean ± SEM. The solid red line is the linear fit to the experimental data (210 ± 60 kJ/mol), and the solid blue line is the linear fit to the simulation data (140 ± 80 kJ/mol). The red and blue shaded regions show the 95% confidence interval of the experimental and simulation fits, respectively, with the overlapping (mauve) region showing the overlap between these two regions. While the <110> HT-$CsPbBr_3$ plane is not observed to be transverse to the wire axis in SAED, the growth rates thus obtained are statistically indistinguishable and further constrain the fit to simulation data. See Figure S16 for further details and for additional simulations on $CsPbI_3$ that are consistent with those shown here.

(C) Snapshots from the MD simulation of phase propagation as a function of time at 267°C, showing the disordered interface between the LT-$CsPbBr_3$ and HT-$CsPbBr_3$ phases. Here, t = 0 ns refers to the earliest simulation time after the initial simulation condition, a pristine interface between the two phases, has equilibrated. Scale bar, 2 nm.

(D) Charge density profiles from the MD simulation at 267°C, obtained by projecting ion positions onto the direction of the wire axis. Data are averaged over a 50-ns time window.

See also Figures S1 and S2.

To reveal the microscopic mechanism of phase propagation, we use electronic structure calculations to parameterize a classical force field for $CsPbBr_3$ crystals (see Tables S1 and S2, Figure S6, and Supplemental Information) and employ this force field in MD simulations. We use $CsPbBr_3$ as a proxy for the mixed halide system because

its simpler composition greatly facilitates the development of a reliable force field. Since both the Br/I and pure Br materials display halide diffusion-limited dynamics, we estimate that the energy scales for defect diffusion and rearrangement in $CsPbBr_3$ and $CsPbIBr_2$ differ by no more than 5%–10%.[35] To further justify our use of the pure Br material in lieu of $CsPbIBr_2$ we have performed additional simulations of $CsPbI_3$ using a different force field. We observe the same transformation mechanisms in both materials, as described below, and activation energies for phase propagation are identical to within the uncertainty of our calculations (see Supplemental Information).

We start our simulations from configurations that include planar interfaces between the LT-$CsPbBr_3$ and HT-$CsPbBr_3$ phases, employing the relative crystallographic orientations suggested by single-area electron diffraction (SAED) ((100) LT-$CsPbBr_3$ abutting (100) HT-$CsPbBr_3$), as seen in Figure 2C. We considered additional interfacial possibilities, such as (110) LT-$CsPbBr_3$ planes abutting (100) HT-$CsPbBr_3$, described further in Supplemental Information. In several long MD simulations at temperatures of 227°C, 247°C, and 267°C we consistently observe growth of the HT-$CsPbBr_3$ phase, in agreement with experiments (Figures S7 and S8; see also Supplemental Information). Propagation rates estimated from at least three independent simulations for each aforementioned interface at each temperature are plotted in Figure 2B. An Arrhenius-type analysis of these data yields an activation energy of 140 ± 80 kJ/mol, and a similar analysis of simulation data at higher temperatures on $CsPbI_3$ (Figures S6, S7, and S9; Tables S1 and S3) is also in reasonable agreement with experiments. A direct comparison of phase-propagation rates obtained at the same temperature in both experiments and simulations remains challenging. Phase propagation at temperatures below 227°C is intractably slow in MD simulations, which cannot exceed the microsecond timescale. On the other hand, the high temperatures used in the simulations are challenging to achieve in the *in situ* CL measurements on account of accentuated damage induced through electron beam irradiation at high temperatures and heat-associated drift.

The simulations reveal the formation of a structurally disordered, liquid-like interfacial layer, characterized by diffusive ion behavior in the interfacial plane (Figure S10). This disorder is the likely origin of the large activation entropy hypothesized from our experiments to partly compensate the substantial measured energetic barrier to advancing the interphase boundary. Large energetic barriers to phase propagation, as measured in our experiments and simulations, can be interpreted as describing activated ion-diffusion events between stoichiometrically different coordination environments. Growth of the HT-$CsPbBr_3$ structure proceeds via diffusion of ions across this disordered interface (Figure 2C and Video S2).[36] Due to the marked structural differences of the two phases, growth cannot proceed layer by layer. In particular, (100) layers of HT-$CsPbBr_3$ have an ionic composition different from that of (100) layers of LT-$CsPbBr_3$. Completion of a new layer of HT-$CsPbBr_3$ thus requires the recruitment of ions from at least two (100) layers of LT-$CsPbBr_3$.

Despite the disordered, liquid-like region between the two phases, using SAED we find the same crystallographic orientation of the HT phase in all nanowires probed rather than a random distribution of crystallographic orientations as might be expected. To rationalize the observation of a preferred crystallographic orientation, we separately compute the distribution of each ion species within the interfacial region in the molecular simulations (Figure 2D). While the positions of the cations are essentially disordered, the positions of the halides remain correlated across the entire liquid-like interface. These correlations manifest as oscillations in the halide

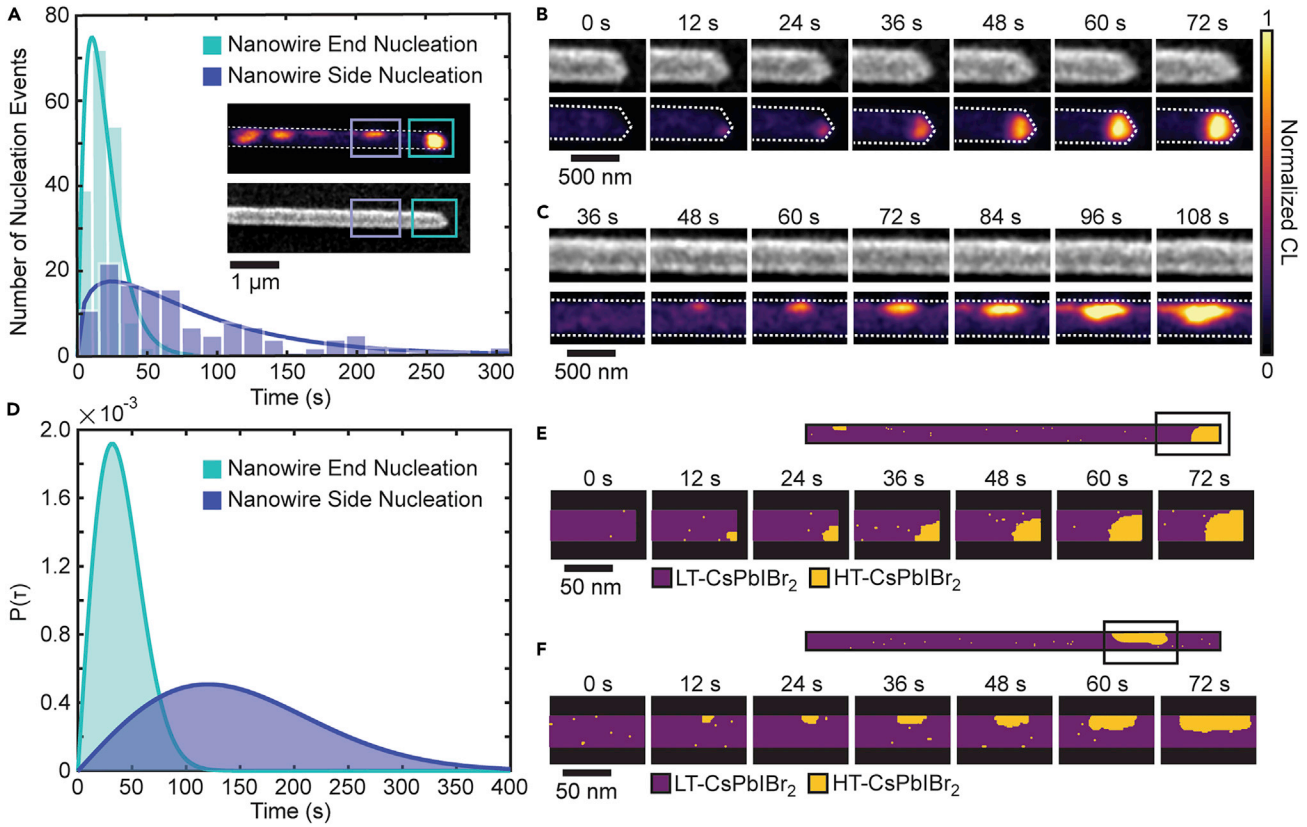

Figure 3. Perovskite Phase Nucleation and Anisotropic Growth from Experiment and Simulation

(A) Plot of observed nucleation events as a function of time for nucleation at nanowire ends (teal) and nucleation at nanowire sides (blue). The inset shows an example of an end nucleation event and a side nucleation event. Scale bar, 1 μm.

(B) Time series of CL and SE images of a single nucleation event at the end of a nanowire. Scale bar, 500 nm.

(C) Time series of CL and SE images of a single nucleation event at the side of a nanowire. Scale bar, 500 nm. An outline of nanowire from the corresponding SE image is shown in the CL images in (B) and (C).

(D) Plot of nucleation probability (P(τ)) as a function of time for nucleation at nanowire ends (teal) and nanowire sides (blue) as a function of time from simulations.

(E) Time series showing a single nucleation event at the nanowire end from simulations. Scale bar, 50 nm.

(F) Time series showing a single nucleation event at the nanowire side from simulations. Scale bar, 50 nm.

See also Figures S11–S14.

density distribution, shown in Figure 2D, and likely act to template the formation of the growing HT phase, dictating its crystallographic orientation despite the incoherent interface. These persistent anionic density correlations are reminiscent of those templating the association of metal nanoparticles in dense ionic solutions.[37]

In our experiments, we observe nucleation of the HT-$CsPbIBr_2$ primarily at nanowire ends; a minority of wires also displays nucleation along the lateral surface. Preferential nucleation on nanowire ends is evident from Figure 3A, which shows a histogram of all nucleation events in ~100 nanowires as a function of time, observed at 163°C (see Supplemental Information and Figure S11 for more details). Here, time zero is defined by the image frame in which we first observe a single HT-$CsPbIBr_2$ phase pixel above the LT-$CsPbIBr_2$ background CL intensity threshold. The distributions of end and side nucleation events are clearly different; the earlier peak of the end nucleation distribution indicates faster nucleation at nanowire ends than sides. To extract a nucleation rate at each of the nanowire ends and sides, we examine distributions of waiting times, which are exponentially distributed, as expected for an

independent, reaction-limited process. We find that nucleation at nanowire ends occurs with a rate of 0.045 s^{-1}, whereas nucleation at wire sides occurs with a rate of 0.013 s^{-1} (Figure S12). This threefold difference likely reflects a higher density of high-energy sites at the wire ends than wire sides owing to the higher density of unterminated bonds at the ends (100) relative to the side surfaces or other exposed facets at wire ends that are not perfectly flat.[38] The nucleation rates at early times are consistent with those inferred at later times using an Avrami analysis,[39] accounting for a constant rate of growth measured independently (see Supplemental Information for details). The inset of Figure 3A shows CL and SE images of part of a single nanowire after nucleation has occurred at the end and side of the nanowire. Time series of the CL and SE images of the nuclei growth at the nanowire end and nanowire side are depicted in Figures 3B and 3C, respectively (Videos S3 and S4). Additional nucleation events are shown in Figure S13. Nucleation at the nanowire end leads to the new phase, expanding until it occupies the full width of the nanowire and then propagating along the long axis of the wire (Figure 3B). Because axial growth can occur in two opposite directions, new regions of HT-$CsPbIBr_2$ formed on the nanowire side are seen to clearly grow asymmetrically with a faster growth rate along the long axis of the nanowire (Figure 3C). By analyzing the extent to which the perovskite phase is circular in the image frames at early times, we find that nucleation at the nanowire sides results in a more anisotropically shaped perovskite phase volume with faster growth along the length of the wire (Figure S14).

We develop a phenomenological model to describe both the preferential location of nucleation sites at the wire end and the anisotropic growth rate at the nanowire side (see Figure S15 and Supplemental Information for additional details). Specifically, we use a simple lattice model of crystal growth with anisotropic bond and surface energies that are greater along the long axes of the wire compared with the short axes. This model phenomenologically accounts for the anisotropy in lattice orientations of the HT-$CsPbIBr_2$ and LT-$CsPbIBr_2$ phases. The lattice is initialized in the pure LT-$CsPbIBr_2$ phase and is instantly quenched to favor the HT-$CsPbIBr_2$ phase. Figure 3D shows two distributions of nucleation events at nanowire ends and nanowire sides from the model, which qualitatively match our experimental results, suggesting that preferential nucleation at nanowire ends is caused by the tendency to minimize interfacial energies between the two phases. Two time series of simulation snapshots of end and side nucleation are shown in Figures 3E and 3F. Growth from the nanowire end proceeds almost isotropically, whereas growth on the nanowire side occurs anisotropically due to the alternation between octahedral double chains and gaps in between them. Specifically, growth occurs at a faster rate in the direction of the lead halide octahedral chains (i.e., along the wire axis); growth in perpendicular directions is noticeably slower. Our MD simulations confirm these anisotropic growth rates: interfaces involving (010) and (001) layers of LT-$CsPbBr_3$, which are parallel to the nanowire axis, display slower average phase propagation compared with orthogonal (100) layers (Figure S16).

The kinetic pathways of the structural phase transition are also apparent in the morphology and photophysical properties of the resulting HT-$CsPbIBr_2$ nanowires. In some cases, when the nanowire is not uniformly contacting the substrate, changes in the nanowire morphology are evident upon the formation of the perovskite phase. As the phase transition proceeds, lattice stress associated with the 7% increase of nanowire volume results in nanowire expansion and bending (Figure S17). Additionally, HT-$CsPbIBr_2$ nanowires with multiple nucleation sites sometimes display dark regions where two phase boundaries meet (Figure S18), suggesting the formation of dislocations with suppressed CL emission.

Conclusion

Through *in situ* dynamic CL imaging and multiscale modeling of the LT-$CsPbIBr_2$ to HT-$CsPbIBr_2$ structural phase transition, we have uncovered the mechanism of the complex, non-martensitic double-chain to perovskite structural transformation in cesium lead halide. The measured activation energy for phase propagation is consistent with a disordered interface between the two phases through which ions must diffuse, as observed in MD simulations. This liquid-like interface is observed far from the melting point of the involved solids and presents strong anion density correlations, which we suspect are responsible for the fixed crystallographic orientation of the nascent perovskite phase within the nanowire, as observed in SAED. The spontaneous formation of an incoherent interface suggests that an ordered solid-solid interface between these two structurally dissimilar phases is thermodynamically less favorable than the sum of LT-$CsPbIBr_2$-liquid and HT-$CsPbIBr_2$-liquid interfaces, plus the concomitant enthalpy required to disorder the interfacial layer, even when such liquid-like configurations are not stable by themselves. Our findings are yet another manifestation of the liquid-like dynamics that have been observed in these highly anharmonic metal halide perovskite lattices that result from the low cohesive energy of their ionic bonds, in contrast to traditional covalent semiconductors.

Our results suggest that similar mechanisms might occur in a large range of materials with disparate structural phases, including other perovskite materials, which crystallize in structures that do not share simple epitaxial interfaces. The experimental method for observing dynamic structural changes introduced in this work could also be extended to other systems, such as 2D transition metal dichalcogenides[40,41] and metal-organic frameworks,[42,43] in which a change in the luminescence intensity or wavelength accompanies a structural change. We expect that similar *in situ* monitoring of phase transitions will significantly aid our ability to characterize phase behavior, enabling quantitative comparison with theoretical results and creating opportunities to manipulate solids and their properties on the nanoscale.

EXPERIMENTAL PROCEDURES

Resource Availability

Lead Contact

Naomi S. Ginsberg (email: nsginsberg@berkeley.edu).

Materials Availability

This study did not generate new unique materials.

Data and Code Availability

All experimental data, computational data, and code are available upon reasonable request to the Lead Contact author.

Low-Temperature Phase $CsPbI_xBr_{3-x}$ Nanowire Synthesis

All of the chemicals were purchased from Sigma-Aldrich unless otherwise stated. PbI_2 (460 mg; 99.999%) was dissolved in 1 mL of anhydrous dimethylformamide and stirred at 70°C overnight before further use. The PbI_2 solution was spun on O_2 plasma-treated glass substrates at 3,000 rpm for 60 s and annealed at 100°C for 15 min. The PbI_2 film was carefully dipped into a glass vial with a mixed solution of 0.4 mL of 8 mg/mL CsI (99.999%)/methanol (anhydrous 99.8%), 1 mL of 8 mg/ CsBr (99.999%)/methanol (anhydrous 99.8%), and 0.8 mL of methanol (anhydrous 99.8%). The PbI_2 side was facing up during the reaction. The reaction was carried out at room temperature for 12 h with the glass vial capped tightly, after which

the substrate was taken out and washed in anhydrous isopropanol for 30 s. The sample was then dried at 50°C for 5 min. The whole growth process took place in a N_2-filled glovebox. The PL emission peak of the corresponding heating transformed high-T phase is the same as that of the $CsPbBr_2I$ composition in our previous report.[9]

Cathodoluminescence Microscopy

CL and SE images were collected with a Zeiss Gemini SUPRA 55 S2 scanning electron microscope modified with a home-built CL detection setup and a home-built heater stage with custom ScopeFoundry software.[44] An aluminum parabolic reflector was positioned above the sample in order to couple a 1.3π sr solid angle of emission into a photomultiplier tube (Hamamatsu, H7421-40) outside of the vacuum chamber. All CL images were acquired with 512 × 512 pixels, a scan rate of ~10 ms/line, a beam current of ~300 pA, and an accelerating voltage of 3.0 kV. The heater is composed of a 0.32-inch diameter O_2 button heater (101275-29, HeatWave Labs) with a thermocouple temperature readout placed adjacent to the sample on an identical Si substrate. For monitoring the phase transition upon heating, the temperature was ramped to an initial set point and then held constant (Figure S4). CL image acquisition was initiated at the initial set point and recorded until the phase transition was complete.

Selected Area Electron Diffraction Measurements

LT-$CsPbIBr_2$ nanowires were transferred by lightly pressing a TEM grid on a nanowire film. Due to the electron dose required in TEM, these measurements cannot be performed *in situ* to, for example, show the different crystal structures of a half-converted nanowire. For HT-$CsPbIBr_2$ nanowires, LT-$CsPbIBr_2$ nanowires were first transferred onto a TEM grid and then heated to induce the phase-transition process in a glovebox. Inside the glovebox, the TEM grid was heated on a hotplate at ~200°C for about 10 min. A temperature higher than the phase-transition temperature was used to ensure the completion of the phase transition, given the possible inefficient thermal transport to nanowires suspended on the TEM grid. The TEM images and SAED patterns in Figure S1 were acquired by using the FEI Titan microscope at the National Center for Electron Microscopy. All measurements were performed at 300 kV.

Continuous Rotation Electron Diffraction Measurements

The dried film was scraped from the glass substrate and then coated on a copper grid with the carbon film (STEM150 Cu grids, Okenshoji) directly. The three-dimensional reciprocal lattices of both low-temperature and high-temperature phases were reconstructed from cRED[45] data (Figure S1). cRED data were collected using a transmission electron microscope (JEOL JEM-2100-LaB_6) operated at an accelerating voltage of 200 kV. The sample was cooled down to −178°C using a cryo-holder filled with liquid N_2. A Gatan Orius camera was used for imaging and locating appropriate crystals for electron diffraction data collection. The cRED data were collected via continuous tilting of the goniometer in the angle range between ±30°. A high-speed hybrid TimePix camera (Amsterdam Scientific Instrument) operated by SoPhy software was used for recording the cRED data. The data were processed using XDS[46] and REDp.[47] TEM bright-field images and energy-dispersive spectra were also collected on the same transmission electron microscope.

SUPPLEMENTAL INFORMATION

Supplemental Information can be found online at https://doi.org/10.1016/j.matt.2020.07.015.

ACKNOWLEDGMENTS

We thank E. Wong, E.S. Barnard, D.F. Ogletree, and S. Aloni at the Molecular Foundry for assistance with CL equipment and helpful discussions. CL and analysis work by C.G.B. and N.S.G. have been supported by STROBE, A National Science Foundation Science & Technology Center under grant no. DMR 1548924. The CL imaging at the Lawrence Berkeley Lab Molecular Foundry and the TEM imaging at the National Center for Electron Microscopy were performed as part of the Molecular Foundry user program, supported by the Office of Science, Office of Basic Energy Sciences, of the US Department of Energy under contract no. DE-AC02-05CH11231. C.G.B. acknowledges an NSF Graduate Research Fellowship (no. DGE1106400), and N.S.G. acknowledges an Alfred P. Sloan Research Fellowship, a David and Lucile Packard Foundation Fellowship for Science and Engineering, and a Camille and Henry Dreyfus Teacher-Scholar Award. Modeling by D.T.L. and materials fabrication and characterization by P.Y. and co-workers is supported under the US Department of Energy, Office of Science, Office of Basic Energy Sciences, Materials Sciences and Engineering Division under contract no. DE-AC02-05-CH11231 within the Physical Chemistry of Inorganic Nanostructures Program (KC3103). The GIWAXS data were collected at the Stanford Synchrotron Radiation Lightsource, SLAC National Accelerator Laboratory, which is supported by the US Department of Energy, Office of Science, Office of Basic Energy Sciences under contract no. DE-AC02-76SF00515. MD simulations have also been partially supported by the National Science Foundation under NSF-REU grant CHE-1659579. The support and resources of the Center for High Performance Computing at the University of Utah are gratefully acknowledged.

AUTHOR CONTRIBUTIONS

C.G.B., M.L., Z.F., D.T.L., M.G., P.Y., and N.S.G. wrote the manuscript. C.G.B., M.L., D.L., D.T.L., P.Y., and N.S.G. conceptualized the experiments. M.L. synthesized the LT-$CsPbIBr_2$ nanowires and performed the PL and XRD measurements. C.G.B. performed the CL experiments and analyzed the CL nucleation and growth data. D.T.L. conceptualized and performed the Ising model simulations. Z.F., P.D., D.T.L., and M.G. conceived the MD simulations and analyzed simulation results. Z.F., P.D., D.D., and M.G. developed the force field and performed MD simulations. A.S.E., J.S., and H.C. collected and analyzed the cRED. T.L. performed the SAED.

DECLARATION OF INTERESTS

The authors declare no competing interests.

Received: May 23, 2020
Revised: July 2, 2020
Accepted: July 8, 2020
Published: August 5, 2020

REFERENCES

1. Green, M.A., Ho-Baillie, A., and Snaith, H.J. (2014). The emergence of perovskite solar cells. Nat. Photonics *8*, 506–514.

2. Stranks, S.D., and Snaith, H.J. (2015). Metal-halide perovskites for photovoltaic and light-emitting devices. Nat. Nanotechnol. *10*, 391–402.

3. McMeekin, D.P., Sadoughi, G., Rehman, W., Eperon, G.E., Saliba, M., Hörantner, M.T., Haghighirad, A., Sakai, N., Korte, L., Rech, B., et al. (2016). A mixed-cation lead mixed-halide perovskite absorber for tandem solar cells. Science *351*, 151–155.

4. Zhang, W., Eperon, G.E., and Snaith, H.J. (2016). Metal halide perovskites for energy applications. Nat. Energy *1*, 1–8.

5. Seok, S.I., Grätzel, M., and Park, N.-G. (2018). Methodologies toward highly efficient perovskite solar cells. Small *14*, 1704177.

6. Eperon, G.E., Paternò, G.M., Sutton, R.J., Zampetti, A., Haghighirad, A.A., Cacialli, F., and Snaith, H.J. (2015). Inorganic caesium lead iodide perovskite solar cells. J. Mater. Chem. A *3*, 19688–19695.

7. Quarti, C., Mosconi, E., Ball, J.M., D'Innocenzo, V., Tao, C., Pathak, S., Snaith, H.J., Petrozza, A., and Angelis, F.D. (2016). Structural and optical properties of methylammonium lead iodide across the tetragonal to cubic phase transition:

implications for perovskite solar cells. Energy Environ. Sci. *9*, 155–163.

8. Wang, T., Daiber, B., Frost, J.M., Mann, S.A., Garnett, E.C., Walsh, A., and Ehrler, B. (2017). Indirect to direct bandgap transition in methylammonium lead halide perovskite. Energy Environ. Sci. *10*, 509–515.

9. Lin, J., Lai, M., Dou, L., Kley, C.S., Chen, H., Peng, F., Sun, J., Lu, D., Hawks, S.A., Xie, C., et al. (2018). Thermochromic halide perovskite solar cells. Nat. Mater. *17*, 261.

10. Dastidar, S., Hawley, C.J., Dillon, A.D., Gutierrez-Perez, A.D., Spanier, J.E., and Fafarman, A.T. (2017). Quantitative phase-change thermodynamics and metastability of perovskite-phase cesium lead iodide. J. Phys. Chem. Lett. *8*, 1278–1282.

11. Sharma, S., Weiden, N., and Weiss, A. (1992). Phase diagrams of quasibinary systems of the type: ABX3-A'BX3; ABX3-AB'X3, and ABX3-ABX'3; X = halogen. Z. Phys. Chem. *175*, 63–80.

12. Swarnkar, A., Marshall, A.R., Sanehira, E.M., Chernomordik, B.D., Moore, D.T., Christians, J.A., Chakrabarti, T., and Luther, J.M. (2016). Quantum dot–induced phase stabilization of α-$CsPbI_3$ perovskite for high-efficiency photovoltaics. Science *354*, 92–95.

13. Wang, Y., Dar, M.I., Ono, L.K., Zhang, T., Kan, M., Li, Y., Zhang, L., Wang, X., Yang, Y., Gao, X., et al. (2019). Thermodynamically stabilized β-$CsPbI_3$-based perovskite solar cells with efficiencies < 18%. Science *365*, 591–595.

14. Steele, J.A., Jin, H., Dovgaliuk, I., Berger, R.F., Braeckevelt, T., Yuan, H., Martin, C., Solano, E., Lejaeghere, K., Rogge, S.M.J., et al. (2019). Thermal unequilibrium of strained black $CsPbI_3$ thin films. Science *365*, 679–684.

15. Faheem, M.B., Khan, B., Feng, C., Farooq, M.U., Raziq, F., Xiao, Y., and Li, Y. (2019). All-inorganic perovskite solar cells: energetics, key challenges and strategies towards commercialization. ACS Energy Lett. *5*, 290–320.

16. Christians, J.A., Habisreutinger, S.N., Berry, J.J., and Luther, J.M. (2018). Stability in perovskite photovoltaics: a paradigm for newfangled technologies. ACS Energy Lett. *3*, 2136–2143.

17. Yi, C., Luo, J., Meloni, S., Boziki, A., Ashari-Astani, N., Grätzel, C., Zakeeruddin, S.M., Röthlisberger, U., and Grätzel, M. (2016). Entropic stabilization of mixed A-cation ABX 3 metal halide perovskites for high performance perovskite solar cells. Energy Environ. Sci. *9*, 656–662.

18. Kong, Q., Lee, W., Lai, M., Bischak, C.G., Gao, G., Wong, A.B., Lei, T., Yu, Y., Wang, L.-W., Ginsberg, N.S., et al. (2018). Phase-transition-induced p-n junction in single halide perovskite nanowire. Proc. Natl. Acad. Sci. U S A *115*, 8889–8894.

19. Dobrovolsky, A., Merdasa, A., Unger, E.L., Yartsev, A., and Scheblykin, I.G. (2017). Defect-induced local variation of crystal phase transition temperature in metal-halide perovskites. Nat. Commun. *8*, 34.

20. Zhu, H., Miyata, K., Fu, Y., Wang, J., Joshi, P.P., Niesner, D., Williams, K.W., Jin, S., and Zhu, X.-Y. (2016). Screening in crystalline liquids protects energetic carriers in hybrid perovskites. Science *353*, 1409–1413.

21. Trots, D.M., and Myagkota, S.V. (2008). High-temperature structural evolution of caesium and rubidium triiodoplumbates. J. Phys. Chem. Solids *69*, 2520–2526.

22. Hanneman, R.E., Banus, M.D., and Gatos, H.C. (1964). High pressure transition in InSb. J. Phys. Chem. Solids *25*, 293–302.

23. Tolbert, S.H., and Alivisatos, A.P. (1994). Size dependence of a first order solid-solid phase transition: the Wurtzite to rock salt transformation in CdSe nanocrystals. Science *265*, 373–376.

24. Murakami, M., Hirose, K., Kawamura, K., Sata, N., and Ohishi, Y. (2004). Post-perovskite phase transition in $MgSiO_3$. Science *304*, 855–858.

25. Zheng, H., Rivest, J.B., Miller, T.A., Sadtler, B., Lindenberg, A., Toney, M.F., Wang, L.-W., Kisielowski, C., and Alivisatos, A.P. (2011). Observation of transient structural-transformation dynamics in a Cu_2S nanorod. Science *333*, 206–209.

26. Lin, Y.-C., Dumcenco, D.O., Huang, Y.-S., and Suenaga, K. (2014). Atomic mechanism of the semiconducting-to-metallic phase transition in single-layered MoS_2. Nat. Nanotechnol. *9*, 391–396.

27. Lai, M., Kong, Q., Bischak, C.G., Yu, Y., Dou, L., Eaton, S.W., Ginsberg, N.S., and Yang, P. (2017). Structural, optical, and electrical properties of phase-controlled cesium lead iodide nanowires. Nano Res. *10*, 1107–1114.

28. Bischak, C.G., Sanehira, E.M., Precht, J.T., Luther, J.M., and Ginsberg, N.S. (2015). Heterogeneous charge carrier dynamics in organic-inorganic hybrid materials: nanoscale lateral and depth-dependent variation of recombination rates in methylammonium lead halide perovskite thin films. Nano Lett. *15*, 4799–4807.

29. Dou, L., Wong, A.B., Yu, Y., Lai, M., Kornienko, N., Eaton, S.W., Fu, A., Bischak, C.G., Ma, J., Ding, T., et al. (2015). Atomically thin two-dimensional organic-inorganic hybrid perovskites. Science *349*, 1518–1521.

30. Dar, M.I., Hinderhofer, A., Jacopin, G., Belova, V., Arora, N., Zakeeruddin, S.M., Schreiber, F., and Grätzel, M. (2017). Function follows form: correlation between the growth and local emission of perovskite structures and the performance of solar cells. Adv. Funct. Mater. *27*, 1701433.

31. Ummadisingu, A., and Grätzel, M. (2018). Revealing the detailed path of sequential deposition for metal halide perovskite formation. Sci. Adv. *4*, e1701402.

32. Bischak, C.G., Hetherington, C.L., Wu, H., Aloni, S., Ogletree, D.F., Limmer, D.T., and Ginsberg, N.S. (2017). Origin of reversible photoinduced phase separation in hybrid perovskites. Nano Lett. *17*, 1028–1033.

33. Bischak, C.G., Wong, A.B., Lin, E., Limmer, D.T., Yang, P., and Ginsberg, N.S. (2018). Tunable polaron distortions control the extent of halide demixing in lead halide perovskites. J. Phys. Chem. Lett. *9*, 3998–4005.

34. Chen, S., Zhang, X., Zhao, J., Zhang, Y., Kong, G., Li, Q., Li, N., Yu, Y., Xu, N., Zhang, J., et al. (2018). Atomic scale insights into structure instability and decomposition pathway of methylammonium lead iodide perovskite. Nat. Commun. *9*, 4807.

35. Lai, M., Obliger, A., Lu, D., Kley, C.S., Bischak, C.G., Kong, Q., Lei, T., Dou, L., Ginsberg, N.S., Limmer, D.T., et al. (2018). Intrinsic anion diffusivity in lead halide perovskites is facilitated by a soft lattice. Proc. Natl. Acad. Sci. U S A *115*, 11929–11934.

36. Peng, Y., Wang, F., Wang, Z., Alsayed, A.M., Zhang, Z., Yodh, A.G., and Han, Y. (2015). Two-step nucleation mechanism in solid-solid phase transitions. Nat. Mater. *14*, 101–108.

37. Zhang, H., Dasbiswas, K., Ludwig, N.B., Han, G., Lee, B., Vaikuntanathan, S., and Talapin, D.V. (2017). Stable colloids in molten inorganic salts. Nature *542*, 328–331.

38. Zhao, B., Jin, S.-F., Huang, S., Liu, N., Ma, J.-Y., Xue, D.-J., Han, Q., Ding, J., Ge, Q.-Q., Feng, Y., et al. (2018). Thermodynamically stable orthorhombic γ-$CsPbI_3$ thin films for high-performance photovoltaics. J. Am. Chem. Soc. *140*, 11716–11725.

39. Chaikin, P.M. (2000). Principles of Condensed Matter Physics (Cambridge University Press).

40. Tongay, S., Zhou, J., Ataca, C., Lo, K., Matthews, T.S., Li, J., Grossman, J.C., and Wu, J. (2012). Thermally driven crossover from indirect toward direct bandgap in 2D semiconductors: $MoSe_2$ versus MoS_2. Nano Lett. *12*, 5576–5580.

41. Bediako, D.K., Rezaee, M., Yoo, H., Larson, D.T., Zhao, S.Y.F., Taniguchi, T., Watanabe, K., Brower-Thomas, T.L., Kaxiras, E., and Kim, P. (2018). Heterointerface effects in the electrointercalation of van der Waals heterostructures. Nature *558*, 425.

42. Silva, C.G., Corma, A., and García, H. (2010). Metal-organic frameworks as semiconductors. J. Mater. Chem. *20*, 3141–3156.

43. Cui, Y., Yue, Y., Qian, G., and Chen, B. (2012). Luminescent functional metal-organic frameworks. Chem. Rev. *112*, 1126–1162.

44. Durham, D.B., Ogletree, D.F., and Barnard, E.S. (2018). Scanning Auger spectromicroscopy using the ScopeFoundry software platform. Surf. Interface Anal. *50*, 1174–1179.

45. Wang, Y., Takki, S., Cheung, O., Xu, H., Wan, W., Öhrström, L., and Inge, A.K. (2017). Elucidation of the elusive structure and formula of the active pharmaceutical ingredient bismuth subgallate by continuous rotation electron diffraction. Chem. Commun. *53*, 7018–7021.

46. Kabsch, W. (2010). XDS. Acta Crystallogr. D Biol. Crystallogr. *66*, 125–132.

47. Wan, W., Sun, J., Su, J., Hovmöller, S., and Zou, X. (2013). Three-dimensional rotation electron diffraction: software RED for automated data collection and data processing. J. Appl. Cryst. *46*, 1863–1873.